ORIGINAL ARTICLE

Processability approach for laser powder bed fusion of metallic alloys

Homero Alberto Castro-Espinosa[1] · Leopoldo Ruiz-Huerta[2,3] ⓘ

Abstract

Processability refers to the ease of achieving the required component while maintaining mechanical performance and processing schedules, which are critical for determining the cost and efficiency of using a given material, from the raw condition to the final product of any manufacturing process. Components built using the laser powder bed fusion with metallic alloys (LPBF-M) process show variability in their mechanical performance, which can be attributed to a range of process parameters and characteristics of the powder material employed by each type of machine. These variations are currently hindering the adoption of this technology at the industrial level. This paper presents a processability approach that could be applied in the LPBF-M to evaluate the possibility of speeding up productivity and minimising the effect on the mechanical properties and relative density and is defined based on the process parameters and powder material characteristics that generate the melting pool and meet bonding criteria at a specific build rate. A case study is carried out with stainless steel 316 (SS316), although this processability analysis could be applied to any other alloy. The results show that a wide range of process parameters generates a suitable processability interval with different values of the build rate. It is also found that slow build rates give rise to less variability in the mechanical properties, while faster rates produce more variability; this is caused by a fast-growing melt pool due to the use of high scan velocities for the SS316 alloy under study.

Keywords Additive manufacturing · Laser powder bed fusion · Processability · Digital manufacturing · Build rate

1 Introduction

Additive manufacturing (AM) enables the fabrication of parts by reducing the number of fabrication steps due to the use of a layerwise construction process, unlike conventional manufacturing processes. The process of powder bed fusion (PBF), a type of AM technology, allows for the fabrication of complex components such as lattice structures, topology-optimised structures, and personalised organic shapes [1, 2]. Depending on the material being processed (polymer or metallic alloys) and the manufacturing machine used, PBF offers different mechanisms for processing the material, which include solid-state sintering, chemically induced binding, liquid phase sintering, and full melting. Most commercial processes primarily utilise liquid phase sintering, such as selective laser sintering (SLS), to process polymers, whereas full melting is used to process metallic alloys, for example, via laser powder bed fusion (LPBF) or electron powder bed fusion (EPBF) [3, 4].

When the LPBF process is applied to metallic alloys (LPBF-M), a source of laser energy with power (P) and scan speed (v) is selectively used to melt micrometric particles of a powder, which are spread over a build plate. The absorbed energy is conducted from the surface to the interior of the powder, forming a hot liquid volume known as a melting pool. In this process, which is based on the conduction, radiation, and convection heat transfer processes, the following thermal phenomena occur: (a) Single melt pools bond with the build plate, which then solidifies and cools rapidly (at a rate 10^6 to 10^8 K/s) [5, 6]. The distance between adjacent laser tracks is referred to as the hatch distance (h_d). (b) These solidified melt pools are adjacent to each other and form a

✉ Leopoldo Ruiz-Huerta
  leoruiz@unam.mx

  Homero Alberto Castro-Espinosa
  homero.castro@icat.unam.mx

[1] Programa de Maestría y Doctorado en Ingeniería, Universidad Nacional Autónoma de México (UNAM), Building "S-Bernardo Quintana Arrioja", 1st floor University City, 04510 Mexico City, Mexico

[2] Instituto de Ciencias Aplicadas y Tecnología, Universidad Nacional Autónoma de México, Circuito Exterior S/N, C.U., Delegación Coyoacán, 04510 Mexico City, Mexico

[3] National Laboratory for Additive and Digital Manufacturing, MADiT, Mexico City, Mexico

layer. (c) Once a complete layer has melted, the build plate is lowered by a predefined distance (known as the layer thickness, l_t), and more powder is spread over the melted layer. This is repeated until a complete component has been built.

In LPBF-M, a laser is used to melt powder contained in a chamber with inert gas. This process involves spot sizes (σ_{spot}) of approximately 50–100 μm, a typical P of 50–400 W, a value for v of 200–2500 mm/s, a value of l_t of 30–60 μm, and particle powder sizes of 20–40 μm. Other technologies use an electron beam rather than a laser as a source of energy to process the material in a vacuum chamber (EPBF-M). In EPBF-M, the σ_{spot} size, P, v, l_t, and powder size are approximately 120–140 μm, up to 3000 W, 3000–42000 mm/s, 50–200 μm, and 40–100 μm, respectively (i.e., higher than those in LPBF [7–11]).

There are a variety of custom-made and commercially available systems for LPBF-M, each with its own manufacturing capabilities that depend on the process parameters used by the system and the characteristics of the powder alloy [12]. The powder alloy shows changes in the temperature gradients, cooling rates, thermal stresses, and dimensions of the melt pool, which could induce defects such as pores and balls that compromise the manufacturing performance of the part. To achieve parts that are free of defects, it is necessary to generate layers consisting of continuous melt pool tracks and healthy thermal conditions. This is achieved by studying the effects of changing the parameters, such as P, v, h_d, and l_t; whenever these parameters are changed, the characteristics of the constructed parts, such as their density, mechanical performance, and surface finish, are modified [12–16].

Additionally, P vs. v diagrams have been created, which allow the identification of different regions. A region free of defects occurs when appropriate values of P vs. v are selected. However, a region of balling defects arises when high values of P and v are chosen, as shown in Fig. 1. When a high P and low v are used, the boiling point temperature is achieved, and the keyhole mode arises, while a low P and high v result in a region with a lack of fusion [20–24].

The energy density (ED), which is defined as $ED = P/v*h_d*l_t$, has been widely studied in regard to LPBF-M with the aim of relating the process parameters to the characteristics of the final components. The ED relation helps in understanding the process in terms of the amount of energy employed, regardless of the material characteristics at different machine parameters. However, it does have some disadvantages, as a given value of ED may be obtained for different combinations of P and v. For example, an h_d of 100 μm and a v of 50 mm/s result in the same value for the linear volumetric ED_v as an h_d of 50 μm and a v of 100 mm/s, where P and l_t are constant, but these ED_V values will give melt pools of different sizes. Another disadvantage is that the mechanical properties resulting from a given
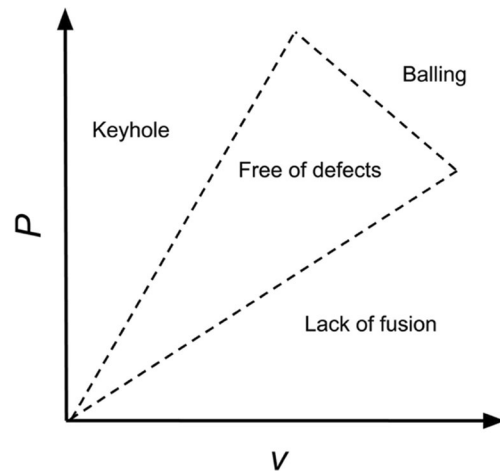

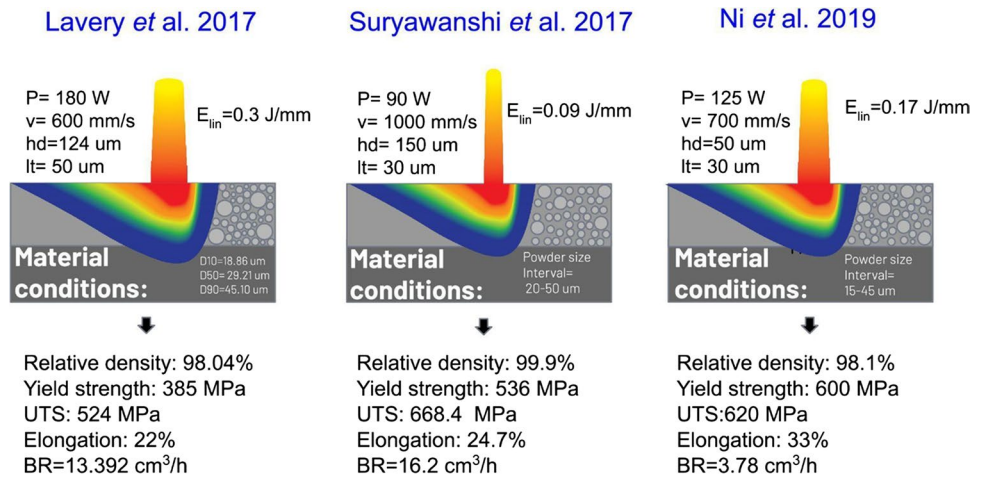
Fig. 1 P vs. v defect diagram [17–19]

ED value are not replicated in another system, even with the same alloy and process parameters but different powder characteristics, meaning that identifying when defects will appear is very difficult [12, 17, 20, 25].

Material characteristics are not included in the ED relation, but they are key in performance variability in terms of the mechanical properties, density, and surface finishing with LPFB-M. For example, Fig. 2 shows the parameters that have been employed by different authors [18, 19, 26] with different types of equipment and the corresponding mechanical property performance of SS316 alloy. It should be noted that with different process parameters, relative densities of up to 98% could be achieved; however, the ED and the mechanical property behaviour were very different in each case, as well as the build rate (BR), which is a measure of the amount of material melted per unit time (defined as $BR = v*h_d*l_t$) [27, 28]. Figure 2 shows that when a given combination of process parameters is applied to the same alloy, the results show variations that depend on the conditions generated during manufacture, such as the ED, making it difficult to determine whether that combination is the best for the processability of the material.

As shown, LPBF-M is a complex manufacturing technology that involves linking material characteristics and selected process parameters by generating intermediate stages, such as melt pools with corresponding temperatures and dimensions, that determine the performance of the built components (i.e., mechanical properties, relative density, roughness, etc.). The process parameters also modify the processing time.

Sisanth et al. [29] defined processability for polymers as "the behaviour and interactions of polymer, filler, oil and other additives during various processing stages, such as mixing, extrusion, calendaring, and moulding process". It has been measured based on parameters such as the cure time, scorch time, viscosity, and extrusion rate.

Fig. 2 Parameters and characteristics of powder material as reported by Lavery et al., Suryawanshi et al., and Ni et al. [18, 19, 26]

Lavery et al. 2017

P= 180 W
v= 600 mm/s
hd=124 um
lt= 50 um

E_{lin}=0.3 J/mm

Material conditions:
D10=18.86 um
D50=29.21 um
D90=45.10 um

↓

Relative density: 98.04%
Yield strength: 385 MPa
UTS: 524 MPa
Elongation: 22%
BR=13.392 cm³/h

Suryawanshi et al. 2017

P= 90 W
v= 1000 mm/s
hd= 150 um
lt= 30 um

E_{lin}=0.09 J/mm

Material conditions:
Powder size Interval= 20-50 um

↓

Relative density: 99.9%
Yield strength: 536 MPa
UTS: 668.4 MPa
Elongation: 24.7%
BR=16.2 cm³/h

Ni et al. 2019

P= 125 W
v= 700 mm/s
hd=50 um
lt= 30 um

E_{lin}=0.17 J/mm

Material conditions:
Powder size Interval= 15-45 um

↓

Relative density: 98.1%
Yield strength: 600 MPa
UTS:620 MPa
Elongation: 33%
BR=3.78 cm³/h

In regard to LPBF-M, a similar concept was proposed by Mukherjee et al. [30]. This author defined printability as "the ability of an alloy to resist distortion, compositional changes and lack of fusion defects" for powder-based AM processes. This concept can be compared with weldability, which is the possibility and ease of welding two alloys [31]. Metallurgic welding technologies, which form the basis of LPBF, have been used to study the LPBF process and to improve it [32]; however, certain differences, such as the use of a higher energy and a continuous medium in welding, make it difficult to apply this approach to a technique such as LPBF, in which a discontinuous material powder alloy is used. Characteristics such as the powder size distribution and morphology have impacts on the laser absorptivity, dynamics and dimensions of the melt pool, cooling rates, and defects and have consequences in terms of the final characteristics of the part, such as its rugosity, relative density, microstructure, and mechanical properties [5, 33–38].

Research studying processability for LPBF-M has been conducted to establish a relationship between densification behaviours, such as defect formation mechanisms, and specific processing parameters [39]. Gu et al. [5] studied the processability of Inconel 718 alloy in terms of the influence of the particle size on the flow behaviour of the powder and the melting and solidification characteristics. They found that smooth melt pool tracks could be created with a powder size of 25 μm, and defects such as balling could be avoided in this way. Engeli et al. [33] studied the processability of IN738LC alloys with different powder sizes in terms of the size of the melt pool, width, porosity, and cracking and concluded that small changes in the composition and size distribution of the powder could strongly affect cracking. Recently, Balba et al. [38] studied processability in relation to density, surface quality, microhardness, and dimensional accuracy with both a fine powder (D50 = 9 μm) and a coarse powder (D50 = 40 μm). They found that with coarse powder, it was possible to achieve higher densities, lower

rugosity, finer microstructures, and higher microhardness. Cosma et al. [40] analysed SS316 via experiments and proposed evaluating the processability based on the quality of construction (i.e., unstable, relatively unstable, and stable processability).

In general, the term *processability* refers to how easily the required processing schedules can be achieved, as stable processing is needed to make production feasible, which is important for determining the cost and efficiency of a given material, from the raw condition to the final product of any manufacturing process. As material processing methods differ considerably from one material to another, the measures used to evaluate these processing methods also vary [41]. For a given material, processability is a performance factor that not only determines the efficiency of industrial production but also plays an essential role in product quality [42]. To the best of our knowledge, processability has not been fully defined and studied in relation to LPBF-M.

In this article, we explore a processability approach and qualitative analysis based on the interaction between the process parameters and the powder material and propose a quantitative approach to processability to ensure that components are free from defects. We also present a case study to validate our approach.

2 Processability

Previous studies of processability have included the interaction between the material characteristics and the process parameters (together or separately) to determine their impacts on density, lack of defects, surface quality, microhardness, and dimensional accuracy. However, no quantitative measurements of this quantity have been proposed; the impact between the process parameters and material characteristics and its impact on productivity have not been considered.

2.1 Proposal of processability for LPBF-M

We consider that once the metallic powder alloy is able to be melted and solidified, there is a wide range of combinations of process parameters that would allow for an increase in the build rate. We therefore propose a definition of the processability for LPBF with metallic alloys as the estimated build rate resulting for free-of-defect components built based on the interaction between the powder metallic alloy and the process parameters, verifying that it meets the application quality requirements.

The authors propose the following steps for quantifying the processability:

1. Identify a safe range of temperatures for free-of-defect construction, which must be between the melting and boiling temperatures, based on the intrinsic properties of the alloy employed.
2. Estimate the temperature that will be reached based on the available machine process parameters (v, P, and spot size) and the material characteristics (such as absorptivity, thermal diffusivity, and thermal conductivity).
3. Estimate the dimensions of the melt pool to propose a suitable hatch distance according to W to calculate the BR based on the v, l_t, and h_d parameters.
4. Verify if the component meets the application quality requirements (such as the mechanical properties, roughness, and relative density) at the selected BR values.

2.2 Analytical background

At the start of the LPBF-M process, a laser spot hits the metal powder; the temperature (T) then rises, and a melting pool is generated as long as the temperature is higher than the melting temperature (T_m). The temperature continues to rise until the maximum value is achieved for the P and v parameters, and it is recommended that T does not exceed the boiling temperature (T_b). Once the maximum

temperature is reached, the material begins to cool down, and the melt pool begins to solidify until the temperature falls below the liquidus temperature [43, 44], as shown in Fig. 3a. Depending on the process parameters, the melting pools achieve a certain depth (D), width (W), and length (L), as shown in Fig. 3b. To estimate the closeness between the generated melt pool and the surrounding solidified material, relations such as D/l_t and h_d/W are used [30, 31, 45].

The melt pool that results from the interaction between the powder metallic alloy and the laser power and scan speed can reach different sizes and temperatures, which define the amount of material that can be melted in a unit of time. The analytical equations utilised in this document for calculating T and melt pool dimensions take into consideration material characteristics, providing a straightforward and efficient implementation. Productivity is determined using a build rate equation that incorporates various process parameters.
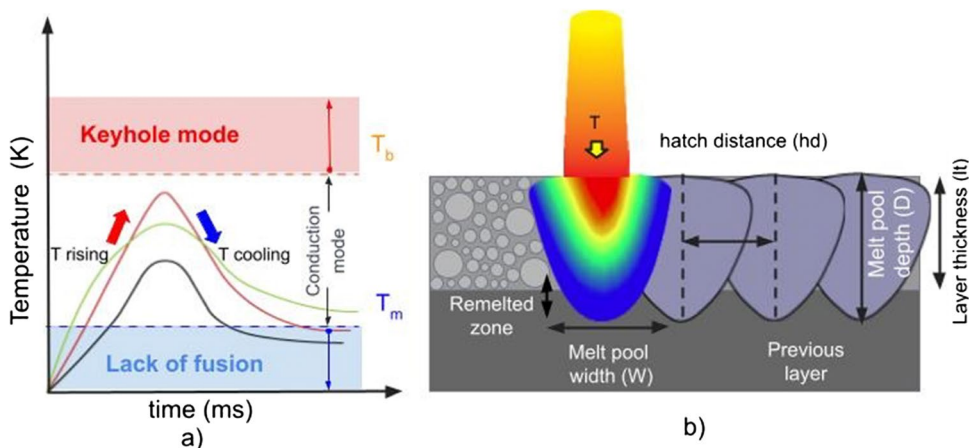
2.2.1 Temperature model

There are several models in the research literature for estimating the temperature during the process of melting a powder by a laser [46–48]. In this work, we use the analytical model presented by King et al. [49], which estimates the temperature reached at the centre of the melt pool as a function of a specific beam size σ_{spot} as follows:

$$T = \frac{\sqrt{2}AI\sigma}{k\sqrt{\pi}}\tan^{-1}\sqrt{\frac{2\alpha}{v\sigma}}, \tag{1}$$

where I is the laser intensity and is calculated as $I = \frac{P}{2\pi\sigma^2}$; A is the absorptivity of the powder material; α is the thermal diffusivity; k is the thermal conductivity; and σ is the laser spot size. This expression can be used to estimate the geometrical dimensions of the Gaussian stationary laser, the limits of the free-of-defect temperature in the LPBF-M process, and the resulting geometrical dimensions of the melt pool.

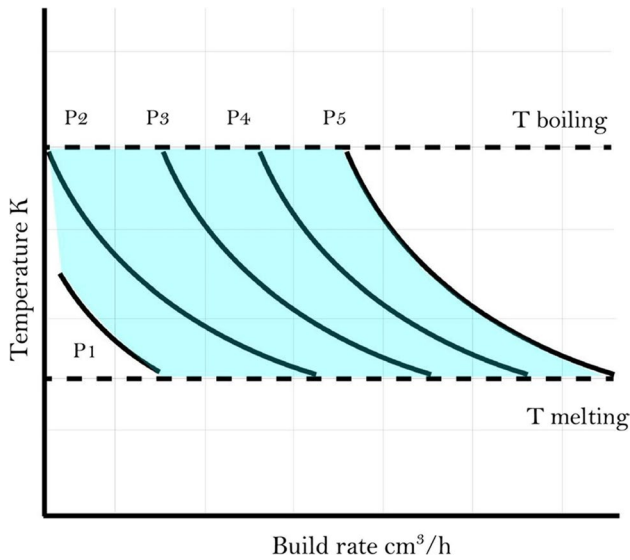**Fig. 3** **a** Temperature behaviour according to time and **b** resulting melting pool

Fig. 4 Processability chart, showing build rate and temperature for different values of P. The areas shown in cyan represent a suitable region for processability

2.2.2 Models for the dimensions of the melt pool

There are models in the literature that can be used to obtain the dimensions of the melt pool based on the size of the laser spot and the thermophysical properties of the material. The model proposed by Tang et al. [50] based on the Rosenthal equation can be employed to predict the melt pool dimensions that, when compared with experimental results, gives an adequate W for the melt pool [45]. This model [50, 51] gives an estimate of the thermal characteristics of the melt pool as follows:

$$T = T_0 + \frac{AP}{2\pi Rk} e^{\frac{-v(\xi+R)}{2\alpha}} \tag{2}$$

where T (K) is the local temperature, T_0 (K) is the temperature inside the chamber, P is the power of the laser (W), v is the scan speed (m/s), k (W/mK) is the thermal conductivity, and α is the thermal diffusivity. R is defined as $R = \xi^2 + y^2 + z^2$ [m] and is the radial distance from the position of the laser, where ξ is the distance from the laser along the direction of travel, y is the distance parallel to the workpiece, and z is the depth below the surface of the workpiece. Simplified approximate expressions were derived from Rosenthal's equation to calculate the width (W) and depth (D) (μm) of the melt pool, as follows [45, 52]:

$$D = \frac{1}{2}W \approx \sqrt{\frac{2AQ}{e\pi\rho C(T-T_0)}} \tag{3}$$

There are many other models [53, 54] that could be used to predict the size of the melt pool. A suitable selection should be considered to find adequate values of the process parameter h_d and the melt pool relation D/l_t.

2.2.3 Build rate

Based on the process parameters v, l_t, and h_d, the BR is calculated using (cm³/h) [27, 28] and is evaluated through

$$BR = v * l_t * h_d \tag{4}$$

2.3 Processability chart

Based on the steps proposed in Sect. 2.1 for quantifying the processability and the equations introduced in Sect. 2.2, processability charts can be generated, as shown in Fig. 4. These charts show the relationship between temperature and BR and indicate the limits defined by the metallic powder

Table 1 Calculations of BR, T, and melt pool relations for the process parameters considered in this study

#	P (W)	v (mm/s)	BR (cm³/h)	T (K)	D (μm)	W (μm)	D/l_t (%)	h_d/W (%)
1	120	750	BR1 14.85	1810.73	51.65	103.31	1.033	1.065
2	140			2112.51	55.79	111.59	1.116	0.986
3	160			2414.30	59.65	119.29	1.193	0.922
4	180			2716.09	63.26	126.53	1.265	0.869
5	200			3017.88	66.69	133.37	1.334	0.825
6	120	857.14	BR2 16.97	1702.60	48.32	96.64	0.966	1.138
7	140			1986.37	52.19	104.38	1.044	1.054
8	160			2270.14	55.79	111.59	1.116	0.986
9	180			2553.91	59.18	118.35	1.184	0.929
10	200			2837.67	62.38	124.76	1.248	0.882
11	120	1000	BR3 19.80	1584.63	44.73	89.47	0.895	1.229
12	140			1848.73	48.32	96.64	0.966	1.138
13	160			2112.84	51.65	103.31	1.033	1.065
14	180			2376.94	54.79	109.58	1.096	1.004
15	200			2641.05	57.75	115.50	1.155	0.952

Fig. 5 Processability chart showing relations between *T* and BR for different process parameters
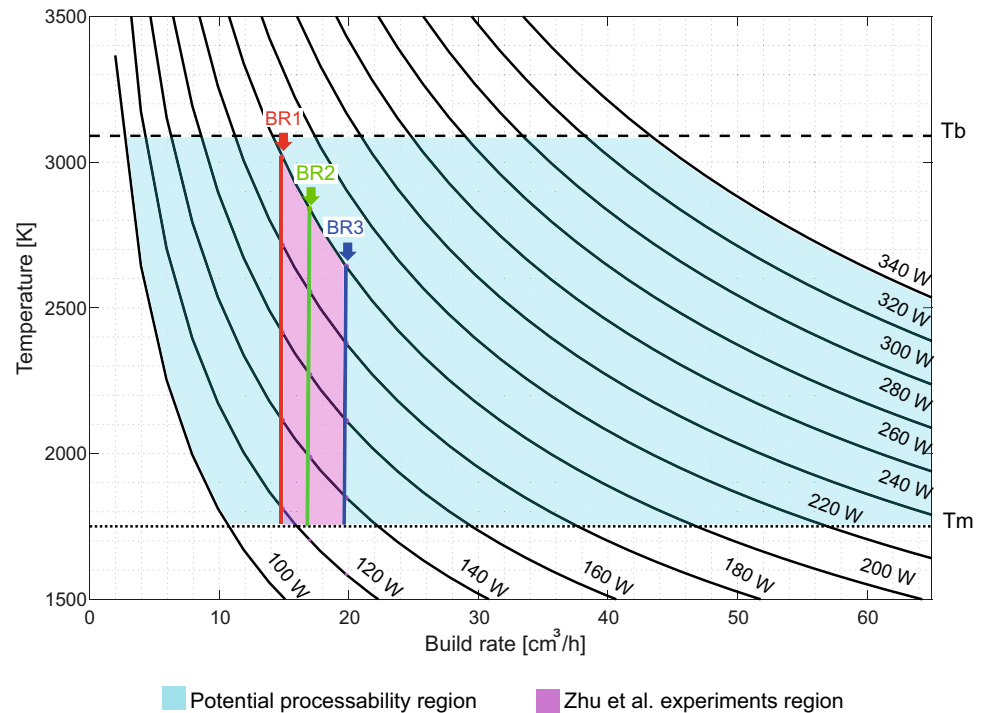
alloy. The potential processing region is highlighted in cyan. The value of *T*, a consequence of the powder alloy characteristics (such as absorptivity, thermal diffusivity, and thermal conductivity) when interacting with the process parameters (such as *P*, *v*, and spot size), is plotted vs. BR for fixed values of h_d and l_t, and it should be greater than T_m but lower than T_b. The processability chart shows the material temperature limits and the parameters that could be used to build a component and their impact on the achievable productivity, but every processability value should be reviewed at different mechanical tests to verify the application quality requirement.

3 Case study

3.1 Materials and methods

To validate the concept of processability proposed in this work, an experimental dataset and results from the literature [55] were used. In this study, a discontinuous laser LPFB-M machine (Renishaw AM250) with a laser spot (σ_{spot}) of 70 µm and wavelength of $\lambda = 1064$ nm was employed under an argon atmosphere with leftover oxygen of 100 ppm in the build chamber. Multiple stainless steel 316 cubes of $10 \times 10 \times 10$ mm were manufactured by Zhu et al. [55] to measure density based on Archimedes' principle using a 0.1 mg electronic balance (Sartorius BSA124S); for this test, the measurement was repeated three times. Based on density measures, the relative

density is estimated as the ratio between the measured density and the literature-reported stainless steel 316 density. Hardness was measured using the same cubes on the top of the surface using a hardness tester (NDT-TIME TMVS-1) applying a load of 500 g.

The tensile strength was determined with an electronic universal tester (CMT5305) according to Chinese Standard No. GB/T 228–2002. The test specimen had a gauge length of 25, and the length, width, and thickness were 50 mm, 4 mm, and 2 mm, respectively. Flexural strength was tested using a CMT4204 universal testing machine according to Chinese Standard No. GB/T 14452–93. Samples had dimensions of $40 \times 6 \times 3$ mm, torsional strength was carried out using a torsion testing machine (NJ-100B), the gauge length was 30 mm, and the overall length and diameter gauge cross sections were 54 mm and 6 mm, respectively. The wear rate was tested using a pin-on-disk rig (Langz-hou Zhongkekei-hua Tech. Co., China) using head pins 6 mm in diameter. According to Zhu et al. [55], discs made of 38CrMoAl were employed in wear tests, and these discs hardened to 0.5 mm depth through iron nitriding (1000 HV hardness). Contact surfaces of pins and discs were polished to an RMS value of Ra ¼ 0.02 mm. Each 30-min test was repeated three times, using a speed of 400 rpm and a rotation radius of 8 mm, with an applied load of 8 N. The Archard equation was used to calculate the wear rate, while pin mass loss was determined by pre- and posttest weighing. Samples were cleaned using acetone after testing. The complete procedures are described in [55]. The mechanical properties were plotted against *T* for three values of BR.

Fig. 6 Behaviour of mechanical properties for varying T and different values of BR: **a** temperature vs. tensile strength, **b** temperature vs. relative density, **c** temperature vs. flexural strength, **d** temperature vs. hardness, **e** temperature vs. torsional strength, and **f** temperature vs. wear rate
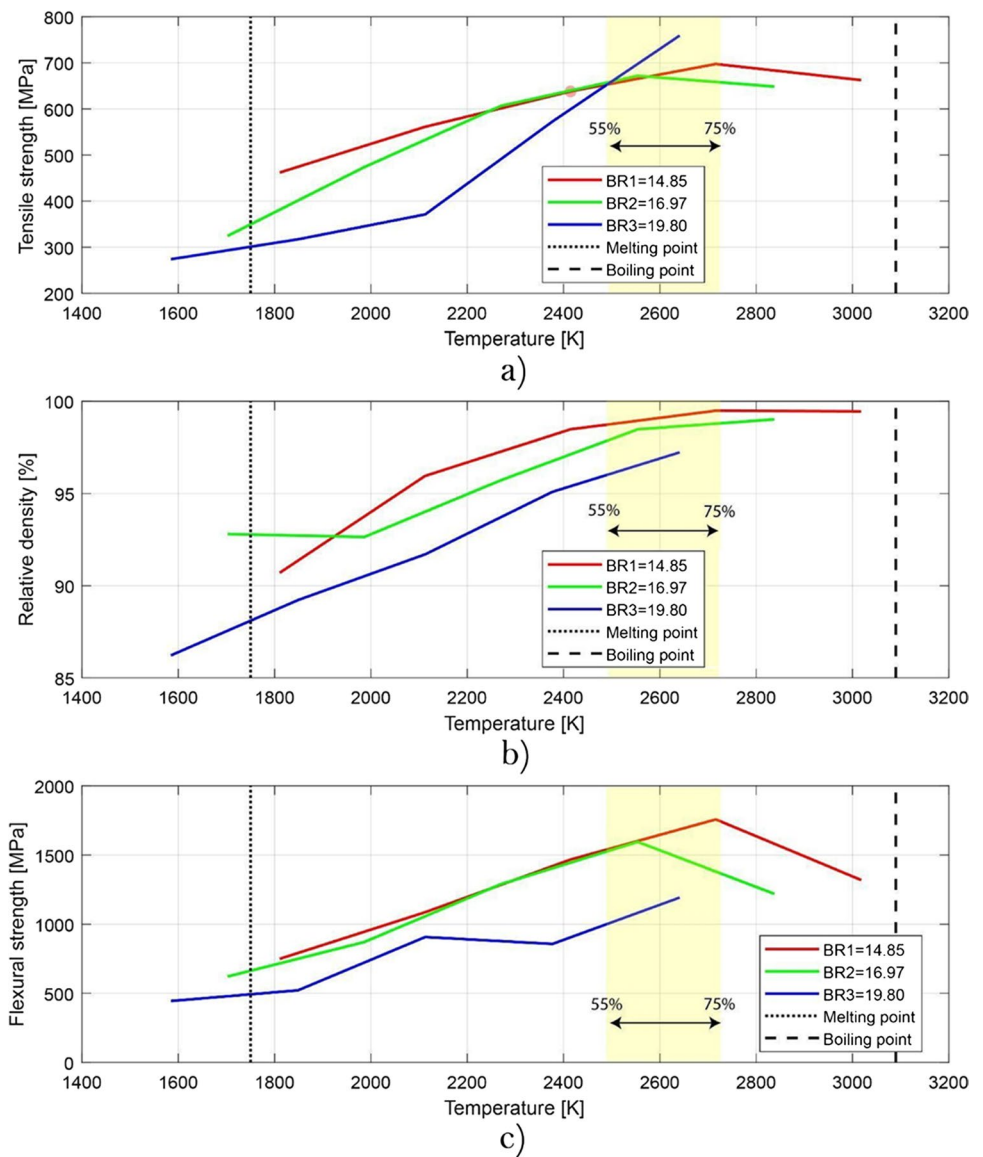

Samples were processed by Zhu et al. [55] with five different levels of laser power (120, 140, 160, 180, and 200 W) and three different exposure times (e_t) of 60, 70, and 80 μs. The process parameters were a hatch distance (h_d) of 110 μm, a point distance p_d of 60 μm, and a l_t of 50 μm. A meander scan strategy was used. v was calculated based on the relation $v = p_d/e_t$. Table 1 shows the calculated BRs based on the estimated scan speeds. The properties of the SS316 alloy used by the authors of the present paper were as follows: absorptivity $A = 0.35$; melting temperature $T_m = 1678$ K; boiling temperature $T_b = 3090$ K; density $\rho = 7800$ kg/m³; thermal conductivity $k = 14$ W/mK;

thermal diffusivity $\alpha = 0.0000039$ m²/s; and heat capacity 450 W/mK [56]. The powder particles were spherical, with sizes in the range of 15 to 45 μm. Processability charts were created based on the BRs against T values. For the process parameters listed above, processability calculations are presented in Table 1. In addition, estimates of the melt pool dimensions and the relations D/l_t and h_d/W are presented.

The processability results are plotted in Fig. 5, and two regions that are suitable for processability are shown. The processability for the process parameters used by Zhu et al. [55] is plotted in magenta, while the potential processing region is highlighted in cyan.

Fig. 7 Behaviour of mechanical properties for varying T and different values of BR: **a** temperature vs. hardness, **b** temperature vs. torsional strength, and **c** temperature vs. wear rate
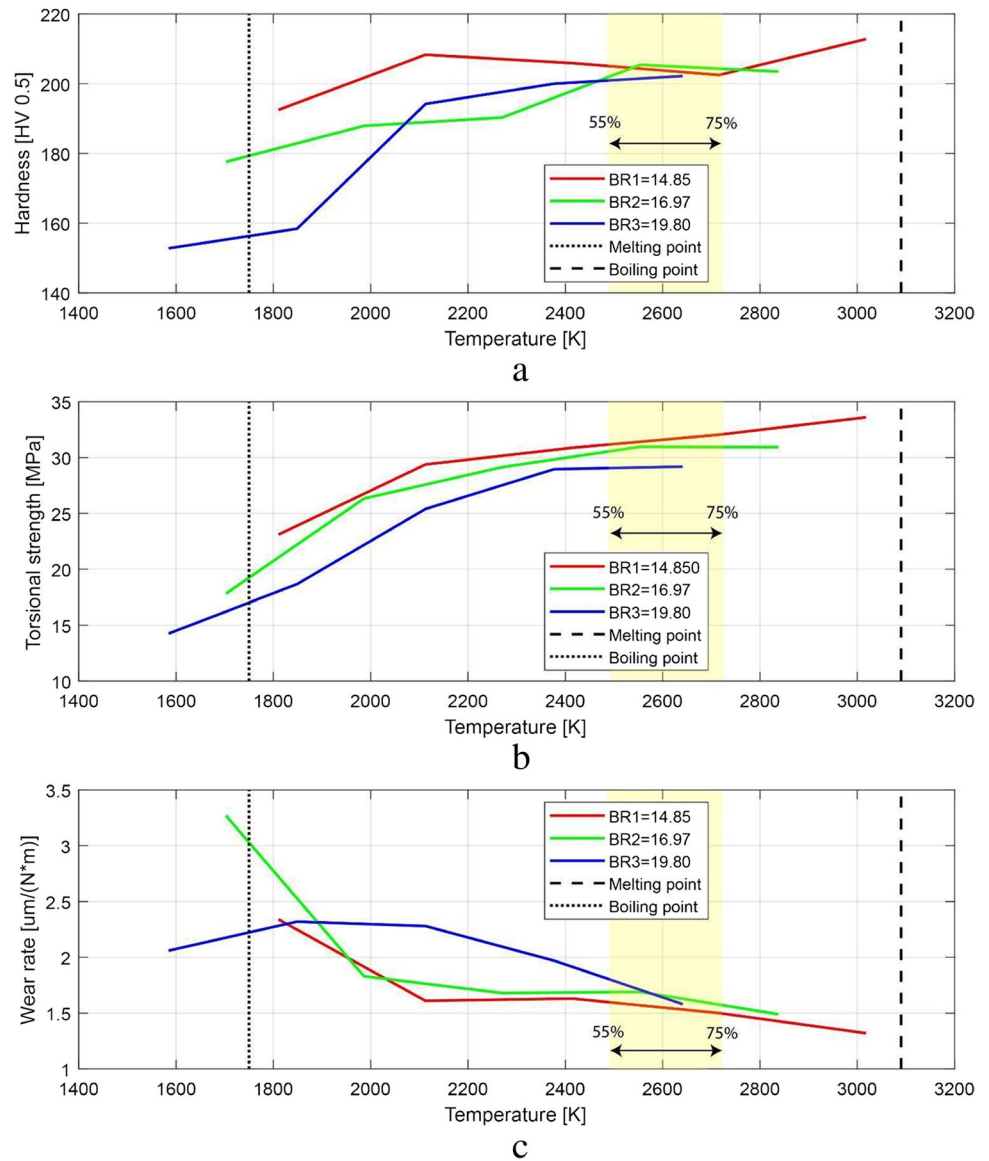
4 Results and discussion

The mechanical properties for the different values of T reached are presented in Figs. 6 and 7 for three different values of BR ($BR_1 = 14.85$ cm^3/h, $BR_2 = 16.97$ cm^3/h, $BR_3 = 19.80$ cm^3/h). It can be seen from the figure that the performance in terms of the relative density, torsional strength, hardness, and wear rate improves as T increases for each value of BR evaluated.

The tensile strength and flexural strength behaviour reach a maximum value (at approximately 55% and 75% of the difference between T_b and T_m) but decrease as the boiling temperature is approached.

It can be observed that the highest tensile strength is achieved for BR_3 (the coldest and fastest conditions of the three). BR_1 and BR_2 operate at a higher T than BR_3, and the

tensile strength diminishes as T_b is approached. Reports in the literature [23] note that operation at higher ED values and beyond the boiling temperature is not recommended for the LPBF-M process, as this generates the keyhole mode and increases porosity in the component.

Figure 6a, b illustrate that the highest relative density is attained when BR1 and BR2 are at their hottest near T_b. However, this does not correspond to higher tensile strength values. Excessive energy increases the thermal gradient and then promotes cracking and microstructural changes, according to Niendorf et al. and Montero et al. [57, 58], who carried out experimental tests for SS316 with P of 400 and 1000 W, showing that the ultimate tensile strength was reduced due to the crystallographic textured columnar coarse grains produced by high P. While the results were dense up to 99%, the mechanical performance of components built at

Table 2 Variability in mechanical performance with BR

	Range of variability (max–min difference)		
	BR$_1$	BR$_2$	BR$_3$
Tensile strength (MPa)	271.46	347.18	485.22
Microhardness HV 0.5	20.3	25.89	49.4
Relative density (%)	8.75	6.22	11.01
Flexural strength (MPa)	569.96	597.69	748.3
Torsional strength (N m)	10.51	13.12	14.93
Wear rate (μg/N*m)	1.02	1.78	0.48

low P was superior to those built at higher P values regarding elongation, tensile strength, yield strength, and hardness; Montero also stated that this decay was due to excessive energy input that promoted cracks propagated in the tensile test direction.

We can see that when T is approximately 2500 K, all of the BRs give similar values for the tensile strength; this suggests that at this temperature, it is possible to increase BR with similar tensile strength as BR$_1$ and BR$_2$. At this value of T, which represents 55% of the range from T_m to T_b, it is possible to explore using a high BR (e.g., BR$_3$) without compromising the tensile strength performance. Higher temperatures could be employed, but high cooling rates would then be present, which would induce cracking behaviour and, hence, a reduction in mechanical performance, as noted by Xiang et al. and Gao et al. [59, 60].

Table 2 shows that low scan speeds (e.g., BR$_1$) are associated with smaller variations in mechanical properties than higher scan speeds (e.g., BR$_2$ and BR$_3$), with the exception of the wear rate.

The model proposed by Tang et al. [50] includes the material properties, and the calculations are simplified compared to finite element and computational fluid simulations; however, at higher linear energy densities, W is narrower than in the experimental results due to the thermal losses that occur during convection and radiation, which are neglected in this model [61]. Hence, another analytical model or scaling law should be used.

Processability involves a complex interplay between several factors, including the T_b and T_m related to the powder alloy and the processing parameters selected, considering and evaluating the potential interactions and trade-offs on mechanical property performance.

5 Conclusions

We have proposed a method of quantifying the processability based on the BR for the LPBF-M process. This metric depends on the process parameters employed and the

characteristics of the material. The results presented here suggest that it is necessary to identify the impact of modifying BR on the mechanical properties. All alloys have different temperature gradients, cooling rates, thermal stresses, and melt pool dimensions due to the variations in the process parameters.

The proposed strategy estimates the temperature of the melt pool during the process based on the characteristics of the metallic alloy powder for particular process parameters (i.e., a particular machine).

Our study of processability suggests that it is possible to speed up the construction by 30% while maintaining similar mechanical properties (hardness, torsional strength, and wear rate) and even improving some properties, such as tensile strength. The concept and analysis of processability presented in this work contribute to the field of LPBF-M by allowing manufacturers to select from a wide range of process parameters and monitor productivity and mechanical property performance. Future work will be required to validate this concept for other alloys and process parameters. We have identified the opportunity to study a widespread of P, v, and h_d combinations, considering the potential of decreasing the build time during manufacturing and the impact on the mechanical properties.

Declarations

References

1. Lin K, Yuan L, Gu D (2019) Influence of laser parameters and complex structural features on the bio-inspired complex thin-wall structures fabricated by selective laser melting. J Mater Process Technol 267:34–43

2. Conner BP, Manogharan GP, Martof AN, Rodomsky LM, Rodomsky CM, Jordan DC et al (2014) Making sense of 3-D printing: creating a map of additive manufacturing products and services. Addit Manuf 1–4:64–76

3. Gebhardt A (2011) Understanding additive manufacturing. Hanser publications Munich, Germany

4. Gibson I, Rosen D, Stucker B (2015) Additive manufacturing technologies: 3D printing, rapid prototyping, and direct digital manufacturing. Springer, New York, NY

5. Gu D, Xia M, Dai D (2019) On the role of powder flow behavior in fluid thermodynamics and laser processability of Ni-based composites by selective laser melting. Int J Mach Tools Manuf 137:67–78

6. Li Y, Gu D (2014) Parametric analysis of thermal behavior during selective laser melting additive manufacturing of aluminum alloy powder. Mater Des 63:856–867

7. Patel S, Vlasea M (2020) Melting modes in laser powder bed fusion. Materialia 9:100591

8. Zhao X, Li S, Zhang M, Liu Y, Sercombe TB, Wang S, et al (2016) Comparison of the microstructures and mechanical properties of Ti–6Al–4V fabricated by selective laser melting and electron beam melting. Mater Des 21–31. https://doi.org/10.1016/j.matdes.2015.12.135

9. Dall'Ava, Dall'Ava, Hothi, Laura D, Henckel, Hart (2019) 3D printed acetabular cups for total hip arthroplasty: a review article. Metals 729. https://doi.org/10.3390/met9070729

10. Pushilina N, Syrtanov M, Kashkarov E, Murashkina T, Kudiiarov V, Laptev R, et al (2018) Influence of manufacturing parameters on microstructure and hydrogen sorption behavior of electron beam melted titanium Ti-6Al-4V alloy. Materials 11. https://doi.org/10.3390/ma11050763

11. Lopez M, Pickett C, Arrieta E, Murr LE, Wicker RB, Ahlfors M, et al (2020) Effects of Postprocess hot isostatic pressing treatments on the mechanical performance of EBM fabricated TI-6Al-2Sn-4Zr-2Mo. Materials 13. https://doi.org/10.3390/ma13112604

12. ScipioniBertoli U, Wolfer AJ, Matthews MJ, Delplanque J-PR, Schoenung JM (2017) On the limitations of volumetric energy density as a design parameter for selective laser melting. Mater Des 113:331–340

13. Yadroitsau I (2009) Selective laser melting: direct manufacturing of 3D-objects by selective laser melting of metal powders. Lambert Academic Publishing

14. Van Humbeeck J (2018) Additive manufacturing of shape memory alloys. Shap Mem Superelasticity 4:309–312

15. Wang Z, Xiao Z, Tse Y, Huang C, Zhang W (2019) Optimization of processing parameters and establishment of a relationship between microstructure and mechanical properties of SLM titanium alloy. Opt Laser Technol 112:159–167

16. Lykov PA (20190 The energy density as a reliable parameter for characterization of selective laser melting of various alloys. Mater Sci Forum 972–977. https://doi.org/10.4028/www.scientific.net/msf.946.972

17. Alfaify AY, Hughes J, Ridgway K (2018) Critical evaluation of the pulsed selective laser melting process when fabricating Ti64 parts using a range of particle size distributions. Addit Manuf 19:197–204

18. Lavery NP, Cherry J, Mehmood S, Davies H, Girling B, Sackett E et al (2017) Effects of hot isostatic pressing on the elastic modulus and tensile properties of 316L parts made by powder bed laser fusion. Mater Sci Eng, A 693:186–213

19. Ni C, Shi Y, Liu J (2018) Effects of inclination angle on surface roughness and corrosion properties of selective laser melted 316L stainless steel. Mater Res Express 6:036505

20. Suzuki A, Nishida R, Takata N, Kobashi M, Kato M (2019) Design of laser parameters for selectively laser melted maraging steel based on deposited energy density. Addit Manuf 28:160–168

21. Guo Q, Zhao C, Qu M, Xiong L, Escano LI, Hojjatzadeh SMH et al (2019) In-situ characterization and quantification of melt pool variation under constant input energy density in laser powder bed fusion additive manufacturing process. Addit Manuf 28:600–609

22. Nayak SK, Mishra SK, Paul CP, Jinoop AN, Bindra KS (2020) Effect of energy density on laser powder bed fusion built single tracks and thin wall structures with 100 μm preplaced powder layer thickness. Opt Laser Technol 125:106016

23. Shrestha S, Starr T, Chou K (2019) A study of keyhole porosity in selective laser melting: single-track scanning with micro-CT analysis. J Manuf Sci Eng 141. https://doi.org/10.1115/1.4043622

24. Kumar P, Farah J, Akram J, Teng C, Ginn J, Misra M (2019) Influence of laser processing parameters on porosity in Inconel 718 during additive manufacturing. Int J Adv Manuf Technol 103:1497–1507

25. Prashanth KG, Scudino S, Maity T, Das J, Eckert J (2017) Is the energy density a reliable parameter for materials synthesis by selective laser melting? Mater Res Lett 5:386–390

26. Suryawanshi J, Prashanth KG, Ramamurty U (2017) Mechanical behavior of selective laser melted 316L stainless steel. Mater Sci Eng, A 696:113–121

27. Gusarov AV, Grigoriev SN, Volosova MA, Melnik YA, Laskin A, Kotoban DV et al (2018) On productivity of laser additive manufacturing. J Mater Process Technol 261:213–232

28. Cacace S, Semeraro Q (2021) Improvement of SLM build rate of A357 alloy by optimizing fluence. J Manuf Process 66:115–124

29. Sisanth KS, Thomas MG, Abraham J, Thomas S (2017) 1 - General introduction to rubber compounding. In: Thomas S, Maria HJ (eds) Progress in Rubber Nanocomposites. Woodhead Publishing, pp 1–39

30. Mukherjee T, Zuback JS, De A, DebRoy T (2016) Printability of alloys for additive manufacturing. Sci Rep 6:19717

31. Eskandari Sabzi H, Rivera-Díaz-Del-Castillo PEJ (2019) Defect prevention in selective laser melting components: compositional and process effects. Materials 12. https://doi.org/10.3390/ma12223791

32. Oliveira JP, Santos TG, Miranda RM (2020) Revisiting fundamental welding concepts to improve additive manufacturing: from theory to practice. Prog Mater Sci 107:100590

33. Engeli R, Etter T, Hövel S, Wegener K (2016) Processability of different IN738LC powder batches by selective laser melting. J Mater Process Technol 229:484–491

34. Pannitz O, Sehrt JT (2020) Transferability of process parameters in laser powder bed fusion processes for an energy and cost efficient manufacturing. Sustain Sci Pract Policy 12:1565

35. Baitimerov R, Lykov P, Zherebtsov D, Radionova L, Shultc A, Prashanth KG (2018) Influence of powder characteristics on processability of AlSi12 alloy fabricated by selective laser melting. Materials 11. https://doi.org/10.3390/ma11050742

36. Brika SE, Letenneur M, Dion CA, Brailovski V (2020) Influence of particle morphology and size distribution on the powder flowability and laser powder bed fusion manufacturability of Ti-6Al-4V alloy. Addit Manuf 100929. https://doi.org/10.1016/j.addma.2019.100929

37. Irrinki H, Dexter M, Barmore B, Enneti R, Pasebani S, Badwe S et al (2016) Effects of powder attributes and laser powder bed fusion (L-PBF) process conditions on the densification

and mechanical properties of 17–4 PH stainless steel. JOM 68:860–868

38. Balbaa MA, Ghasemi A, Fereiduni E, Elbestawi MA, Jadhav SD, Kruth J-P (2021) Role of powder particle size on laser powder bed fusion processability of AlSi10mg alloy. Addit Manuf 37:101630

39. Tan Q, Liu Y, Fan Z, Zhang J, Yin Y, Zhang M-X (2020) Effect of processing parameters on the densification of an additively manufactured 2024 Al alloy. J Mater Sci Technol 58:34–45

40. Cosma C, Kessler J, Gebhardt A, Campbell I, Balc N (2020) Improving the mechanical strength of dental applications and lattice structures SLM processed. Materials 13. https://doi.org/10.3390/ma13040905

41. Kalinchev EL (2002) Controlling the processability of polymeric materials. Int Polym Sci Technol 29:55–62

42. Cai J, Liu Z, Cao B, Guan X, Liu S, Zhao J (2020) Simultaneous improvement of the processability and mechanical properties of polyamide-6 by chain extension in extrusion. Ind Eng Chem Res 59:14334–14343

43. Greenwald LE, Breinan EM, Kear BH (1979) Heat transfer properties and microstructures of laser surface melted alloys. AIP Conf Proc 50:189–204

44. Ansari MJ, Nguyen D-S, Park HS (2019) Investigation of SLM process in terms of temperature distribution and melting pool size: modeling and experimental approaches. Materials 12. https://doi.org/10.3390/ma12081272

45. Tang M, Chris Pistorius P, Beuth JL (2017) Prediction of lack-of-fusion porosity for powder bed fusion. Addit Manuf 39–48. https://doi.org/10.1016/j.addma.2016.12.001

46. Ning J, Mirkoohi E, Dong Y, Sievers DE, Garmestani H, Liang SY (2019) Analytical modeling of 3D temperature distribution in selective laser melting of Ti-6Al-4V considering part boundary conditions. J Manuf Process 44:319–326

47. Yang Y, Knol MF, van Keulen F, Ayas C (2018) A semi-analytical thermal modelling approach for selective laser melting. Addit Manuf 21:284–297

48. Li JF, Li L, Stott FH (2004) Comparison of volumetric and surface heating sources in the modeling of laser melting of ceramic materials. Int J Heat Mass Transf 47:1159–1174

49. King WE, Barth HD, Castillo VM, Gallegos GF, Gibbs JW, Hahn DE et al (2014) Observation of keyhole-mode laser melting in laser powder-bed fusion additive manufacturing. J Mater Process Technol 214:2915–2925

50. Tang M, Pistorius PC, Narra S, Beuth JL (2016) Rapid solidification: selective laser melting of AlSi10Mg. JOM 68:960–966

51. Promoppatum P, Yao S-C, Pistorius PC, Rollett AD (2017) A comprehensive comparison of the analytical and numerical prediction of the thermal history and solidification microstructure of Inconel 718 products made by laser powder-bed fusion. Proc Est Acad Sci Eng 3:685–694

52. Chen Q, Zhao Y, Strayer S, Zhao Y, Aoyagi K, Koizumi Y et al (2021) Elucidating the effect of preheating temperature on melt pool morphology variation in Inconel 718 laser powder bed fusion via simulation and experiment. Addit Manuf 37:101642

53. Fabbro R (2019) Scaling laws for the laser welding process in keyhole mode. J Mater Process Technol 264:346–351

54. Rubenchik AM, King WE, Wu SS (2018) Scaling laws for the additive manufacturing. J Mater Process Technol 257:234–243

55. Zhu Y, Peng T, Jia G, Zhang H, Xu S, Yang H (2019) Electrical energy consumption and mechanical properties of selective-laser-melting-produced 316L stainless steel samples using various processing parameters. J Clean Prod 77–85. https://doi.org/10.1016/j.jclepro.2018.10.109

56. Diaz Vallejo N, Lucas C, Ayers N, Graydon K, Hyer H, Sohn Y (2021) Process optimization and microstructure analysis to understand laser powder bed fusion of 316L stainless steel. Metals 11:832

57. Montero-Sistiaga ML, Godino-Martinez M, Boschmans K, Kruth J-P, Van Humbeeck J, Vanmeensel K (2018) Microstructure evolution of 316L produced by HP-SLM (high power selective laser melting). Addit Manuf 23:402–410

58. Niendorf T, Leuders S, Riemer A, Richard HA, Tröster T, Schwarze D (2013) Highly anisotropic steel processed by selective laser melting. Metall Mater Trans B 44:794–796

59. Xiang Z, Yin M, Dong G, Mei X, Yin G (2018) Modeling of the thermal physical process and study on the reliability of linear energy density for selective laser melting. Results Phys 9:939–946

60. Gao P, Huang W, Yang H, Jing G, Liu Q, Wang G et al (2020) Cracking behavior and control of β-solidifying Ti-40Al-9V-0.5Y alloy produced by selective laser melting. J Mater Sci Technol 39:144–154

61. Hekmatjou H, Zeng Z, Shen J, Oliveira JP, Naffakh-Moosavy H (2020) A comparative study of analytical rosenthal, finite element, and experimental approaches in laser welding of AA5456 alloy. Metals 10:436